Deuteron-nucleus collisions in a multiphase transport model

Zi-wei Lin
Physics Department, The Ohio State University, Columbus, Ohio 43210, USA

Che Ming Ko
Cyclotron Institute and Physics Department, Texas A&M University, College Station, Texas 77843, USA
(Received 8 January 2003; published 26 November 2003)

Using a multiphase transport model, we study pseudorapidity distributions and transverse momentum spectra in deuteron-gold collisions at RHIC. We find that final-state partonic and hadronic interactions affect the transverse momentum spectrum of protons more than those of kaons or pions. Relative to $p+p$ collisions at same center-of-mass energy per nucleon pair, the effect of final-state interactions on the charged particle transverse momentum spectra in d+Au collisions is much smaller than observed in experimental data, indicating that initial-state effects such as the Cronin effect are important.

DOI: 10.1103/PhysRevC.68.054904 PACS number(s): 25.75.−q, 24.10.Lx

I. INTRODUCTION

To study heavy ion collisions at the Relativistic Heavy Ion Collider (RHIC) at Brookhaven National Laboratory, in which a deconfined plasma of quarks and gluons is expected to be formed, we have developed a multiphase transport (AMPT) model that includes both final-state partonic and hadronic interactions [1–3]. The model has been very useful for understanding various observables in Au+Au collisions at RHIC such as the rapidity and transverse momentum distributions of various particles [1–3] as well as charmonium [4] and strangeness [5] productions. In particular, it allows one to study both thermal and chemical equilibration in the partonic and hadronic matter formed in these collisions. The AMPT model has also been extended to include the string melting mechanism [6,7], in which soft strings produced from initial nucleon-nucleon interactions are converted directly to partons, in order to explain the measured elliptic flow [8] and two-pion correlation functions [9] at RHIC.

In spite of its success, the AMPT model has many uncertainties in its input physical parameters, particularly those related to the initial conditions introduced to the model. For example, the number of initial minijet partons in the AMPT model, that is given by the hard processes from the Heavy Ion Jet INteraction Generator (HIJING) model [10–12], depends on the nuclear shadowing, i.e., the modification of the parton distributions in a nucleon when it is in a nucleus. As a result, the final particle multiplicity produced in relativistic heavy ion collisions is affected by nuclear shadowing [2,3]. The production of high p_T particles or hadrons made of heavy quarks, which is described by perturbative QCD processes, is even more sensitive to the nuclear shadowing effect. Furthermore, other nuclear effects such as the Cronin effect [13], which set in already in *p-A* collisions, need to be included. The uncertainties in the initial condition also exist in other transport models with partonic degrees of freedom [14,15] as well as theoretical models such as the hydrodynamical model [16–19] and the QCD saturation model [20–24].

Since final-state interactions (FSI) are expected to be less important in deuteron-gold collisions than in collisions between heavy nuclei, both the Cronin effect and the nuclear shadowing effect (e.g., through dilepton measurements [25]) can be better studied in these collisions. Improved knowledge on these effects are useful for making reliable theoretical interpretations of the observations in heavy ion collisions at RHIC. In this paper, we use the AMPT model to study the global observables in deuteron-gold collisions such as the pseudorapidity distributions and the transverse momentum spectra. Because of the small interaction volume in $d+$Au collisions, we use the default AMPT model, i.e., without the string melting mechanism, in the present study, as the initial energy density produced in these collisions is expected to be small.

This paper is organized as follows. In Sec. II, we briefly review the AMPT model. Results from the AMPT model on deuteron-gold collisions at RHIC are then shown in Sec. III, with the charged particle pseudorapidity distributions and their centrality dependence given in Sec. III A, the transverse momentum spectra of different particles in Sec. III B, and the effects due to modifications of the string fragmentation parameters and nuclear shadowing in Sec. III C. A summary is then given in Sec. IV. Finally, the effect of centrality selection on the centrality dependence of charged particle pseudorapidity distributions is discussed in the Appendix.

II. THE AMPT MODEL

The AMPT model is a hybrid model that consists of four components: the initial conditions, the parton cascade, the conversion from partonic to hadronic matter, and the hadron cascade. In the default AMPT model [1–5], the initial conditions are generated from the HIJING model [10–12] (version 1.383 for this study), which usually uses a Woods-Saxon radial shape for the colliding nuclei and introduces a parametrized nuclear shadowing function that depends on the impact parameter of the collision [10]. Interactions among minijet partons, which are produced from initial hard nucleon-nucleon interactions, are modeled by the Zhang's parton cascade (ZPC) [14]. After partons stop interacting, they recombine with their parent strings, which are produced

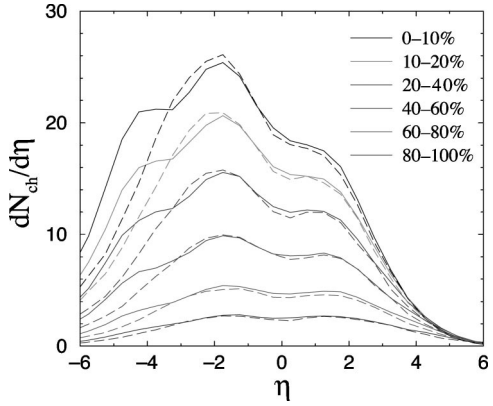

FIG. 1. Pseudorapidity distributions of charged particles in d+Au collisions at $\sqrt{s_{NN}}$=200 GeV with centralities determined from $N_{\rm part}$. Solid and dashed curves represent results from the AMPT model and the HIJING model (without quenching), respectively.

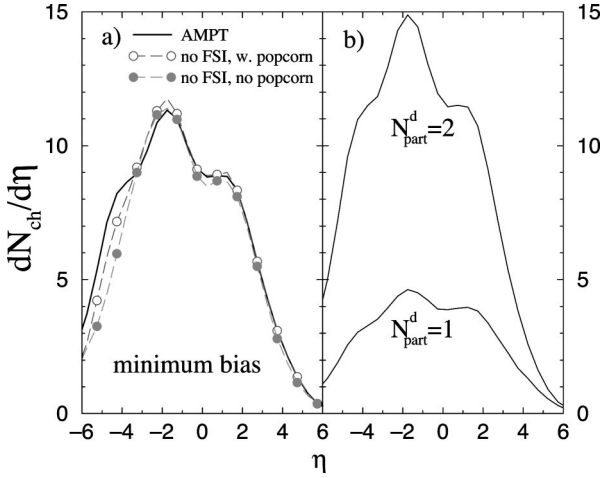

FIG. 2. Pseudorapidity distributions of charged particles (a) for minimum-bias events when different interactions are included and (b) for events from AMPT with $N_{\rm part}^{\rm d}$=2 and with $N_{\rm part}^{\rm d}$=1.

from initial soft nucleon-nucleon interactions, and fragment to hadrons according to the Lund string fragmentation model [26,27]. Dynamics of resulting hadronic matter is then described by a hadronic cascade based on the relativistic transport (ART) model [28]. Final hadronic observables including contributions from the strong decay of resonances are determined when the hadronic matter freezes out.

In this study, we use the Hulthen wave function [29] to model the structure of a deuteron [30]:

$$u(r) = Ce^{-\alpha r}(1 - e^{-\mu r}), \tag{1}$$

where r represents the relative distance between the proton and neutron in the deuteron, the normalization constant C is determined from $\int_0^\infty u(r)^2 dr = 1$, and the small D-wave contribution ($\sim$6%) to the deuteron wave function is neglected. With $\alpha = (4.38\ \text{fm})^{-1}$ and $\mu = (1.05\ \text{fm})^{-1}$, the root-mean-square radius of the deuteron, $\sqrt{\langle r^2\rangle}/2$, is 2.0 fm, consistent with the measured value.

III. AMPT RESULTS ON DEUTERON-GOLD COLLISIONS

We have studied deuteron-gold collisions at $\sqrt{s_{NN}}$ =200 GeV with both deuteron and gold having the same energy of 100 GeV per nucleon. In this study, "minimum-bias" d+Au events are defined as those within the impact parameter range between 0 and 12 fm, and they are separated into different centrality bins.

A. Pseudorapidity distributions of charged particles

Figure 1 shows the pseudorapidity distributions of charged particles in the six centrality bins of 0–10%, 10–20%, 20–40%, 40–60%, 60–80%, and 80–100%. Here, the centrality is determined according to the value of $N_{\rm part}$, i.e., the total number of participants in both deuteron and gold nuclei, in each event. The pseudorapidity in this study is evaluated in the nucleon-nucleon center-of-mass frame, and negative rapidities correspond to the fragmentation region of the gold nucleus. Solid curves are results from the AMPT model, while dashed curves are those from the HIJING model without quenching. Note that the AMPT model without final-state partonic and hadronic interactions is equivalent to the HIJING model without jet quenching if the popcorn mechanism [31] in the PYTHIA/JETSET program [26] is treated in the same way. It is seen that the asymmetry in the pseudorapidity distributions, e.g., by comparing values of $dN_{ch}/d\eta$ at $\eta=-2$ and $\eta=+2$, decreases as collisions become less central, and the pseudorapidity distribution for the most peripheral bin is almost symmetric. As expected, final-state interactions in d+Au collisions have a smaller effect on charged particle pseudorapidity distributions than in the case of central heavy ion collisions at RHIC [2,3].

We note that the appearance of small bumps around $\eta\sim-4$ is mainly due to interactions of produced particles with initial incoming nucleons in the gold nucleus, which has an initial half width of $R_{\rm Au}/\gamma$ in the longitudinal direction with $R_{\rm Au}$ being the hard-sphere radius of the gold nucleus and γ denoting the Lorentz boost factor of a nucleon in the nucleon-nucleon center-of-mass frame. If the initial half width is reduced by a factor of 5, the charged particle pseudorapidity distributions would be smooth around $\eta\sim-4$ and also have slightly lower values in the region of $-6<\eta<-3$.

Figure 2(a) shows the pseudorapidity distributions of charged particles for minimum-bias d+Au events. Solid curves are results from the AMPT model, dashed curves with open circles are AMPT results without final-state interactions, and dashed curves with filled circles are those without both final-state interactions and the popcorn mechanism for baryon-antibaryon production [1–3]. We see that both final-state interactions and the popcorn mechanism broaden the pseudorapidity distributions, especially in the fragmentation region of the gold nucleus, leading thus to a moderate increase of the particle multiplicity in the region of $-6<\eta<-3$. We note that without final-state interactions and the popcorn mechanism, results from the AMPT model are equivalent to those from the HIJING model (without jet quenching) as same values of a and b in Eq. (2) are used.

One can separate events according to the number of participants from the deuteron, i.e., $N_{\rm part}^{\rm d}$. As an example, Fig.

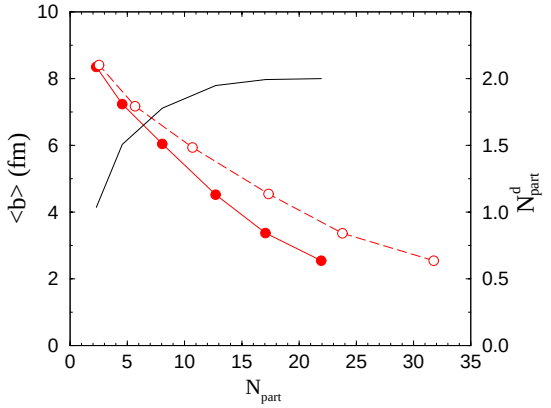

FIG. 3. The average value of impact parameter (in fm) and N^{d}_{part} (solid curve) as a function of the total N_{part}. See text for details.

2(b) shows the pseudorapidity distributions of charged particles from the AMPT model for events with one or two nucleon(s) from the deuteron that are involved in primary collisions. About 2/3 of minimum-bias events from the AMPT model have $N^{d}_{part}=2$ with average values of N^{Au}_{part} at 10.4 and the mean impact parameter at 4.7 fm. On the other hand, for events with $N^{d}_{part}=1$, the average value of N^{Au}_{part} is 2.8 and the mean impact parameter is 7.8 fm.

In Fig. 3, we show by the solid curve with circles the average impact parameter as a function of the average value of N_{part} at each centrality bin. Here, the number of participants is defined as the number of initial (projectile and target) nucleons involved in *primary* collisions, i.e., not including those initial nucleons that interact with produced particles in the final state. The solid curve with no symbols in Fig. 3 represents N^{d}_{part}. We see that N^{d}_{part} increases toward the value of 2 rather quickly from peripheral to central collisions. The dashed curve with open circles shows the number of participating nucleons that also include initial nucleons that are involved in final-state interactions. It is seen that final-state interactions increase the number of participating nucleons by more than 40% for the most central events (0–10% centrality bin). However, since the energies involved in final-state interactions are much lower than those in the primary collisions, they contribute much less to particle production. In this study, we thus only include initial nucleons that are involved in primary collisions for determining N_{part}.

The centrality dependence of particle multiplicity and transverse energy at mid-pseudorapidities ($-0.5<\eta<0.5$) are shown in Fig. 4. The solid curve and the dashed curve with open squares represent, respectively, $(dN_{ch}/d\eta)/N_{part}$ and $(dE_T/d\eta)/N_{part}$, where E_T includes the contribution from neutral particles. In this study, $E_T=E\sin\theta$ with θ being the polar angle, and E is defined as the kinetic energy for baryons, the total energy including the mass for anti-baryons, and the total energy for all other particles. We observe that both the particle multiplicity and transverse energy per participant gradually decrease with increasing N_{part}. However, we shall see in Sec. III C and the Appendix that this moderate decrease with centrality will change when centralities are determined differently or when the string fragmentation function is modified in more central d+Au collisions. Fig. 4 also shows that the ratio of the transverse energy and particle multiplicity per participant (solid curve with filled squares), i.e., the average transverse energy per charged particle, is rather flat. Also shown by the solid curve with triangles is the mean transverse momentum of charged particles, which is seen to change little with N_{part} as well.

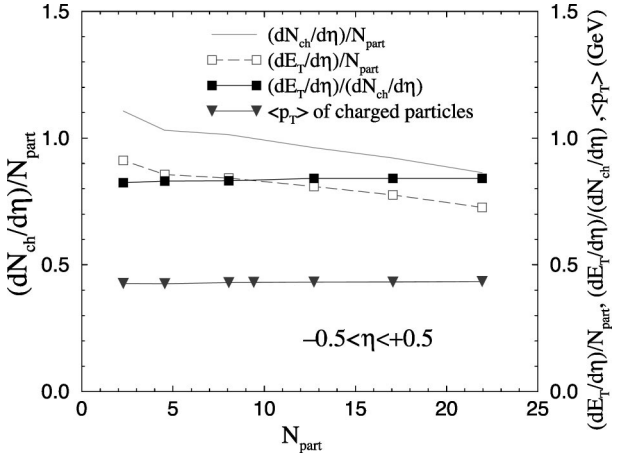

FIG. 4. Centrality dependences of charged particle multiplicity and transverse energy (in GeV) per participant, the mean transverse energy (in GeV) per charged particle, and the mean p_T (in GeV/c) of charged particles at midpseudorapidity.

The centrality dependence of the charged particle multiplicity per participant at different pseudorapidities is shown in Fig. 5, where the value at each η represents the average value within the pseudorapidity range of $\eta\pm0.5$. We see an increase of this quantity at the backward pseudorapidity $\eta=-4$ (curve with open diamonds) and a fast decrease at the forward pseudorapidity $\eta=+4$ (curve with filled diamonds). Furthermore, the decrease with centrality becomes stronger as the pseudorapidity changes from negative values to more positive values. These are consistent with the picture that multiple interactions in the gold nucleus push particle pro-

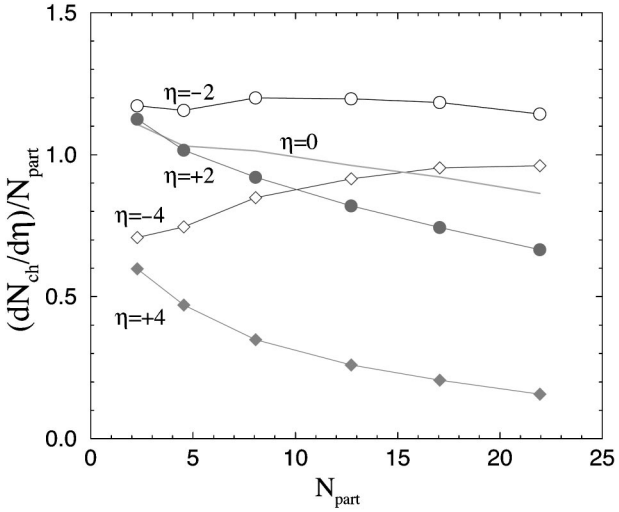

FIG. 5. Centrality dependence of charged particle multiplicity per participant at different pseudorapidities.

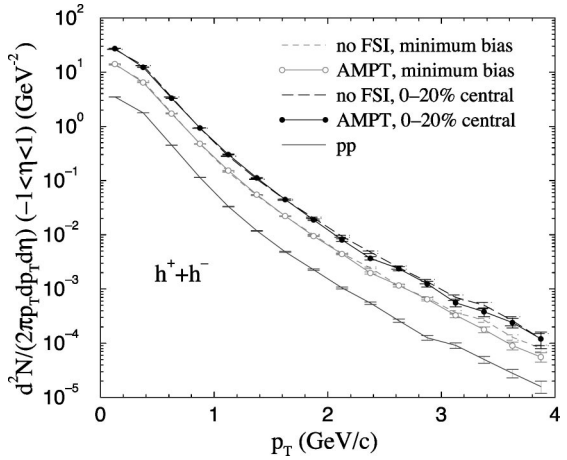

FIG. 6. Transverse momentum spectra of charged particles within $-1<\eta<1$ for d+Au collisions from AMPT with (solid curves with circles) or without (dashed) final-state interactions. The solid curve is the AMPT result for $p+p$ collisions at the same center-of-mass energy per nucleon pair.

ductions toward the negative rapidity region. Since we find that the mean transverse energy per charged particle at a given pseudorapidity does not change much with centrality, the centrality dependence of $(dE_T/d\eta)/N_{\rm part}$, i.e., the transverse energy per participant, has a similar behavior at each pseudorapidity as $(dN_{ch}/d\eta)/N_{\rm part}$.

B. Transverse momentum spectra

The transverse momentum spectra of charged particles in the pseudorapidity range of $-1<\eta<1$ for both minimum-bias and 0–20% central d+Au collisions are shown in Fig. 6. Solid curves with circles are results from the AMPT model while dashed curves are those without final-state partonic and hadronic interactions. For comparisons, the AMPT results for minimum-bias $p+p$ collisions are shown by the solid curve. In all transverse momentum distributions and their ratios shown later, we include the statistical errors in the AMPT model, which become large at moderately high p_T.

To better examine the distributions shown in Fig. 6, ratios of the p_T spectra of charged particles from d+Au collisions over those from minimum-bias $p+p$ collisions are shown in Fig. 7. We see that, even without final-state partonic and hadronic interactions, the ratios (dashed curves) are not flat but instead tend to increase with p_T in the range of 0–3 GeV/c shown in the figure. This behavior is mainly a result of different scalings for hard and soft processes with respect to the number of binary collisions in the initial conditions from the HIJING model. While particle production at high enough p_T scales with the number of initial binary collisions, low momentum particles have a weaker dependence. Final-state interactions further modify the ratios of p_T spectra, as seen from comparisons between the solid and dashed curves.

Recently, the transverse momentum spectra of charged particles in d+Au collisions have been measured at RHIC [32]. Compared with the experimental data at $0<p_T<3$ GeV/c, the p_T dependence of the ratios from the

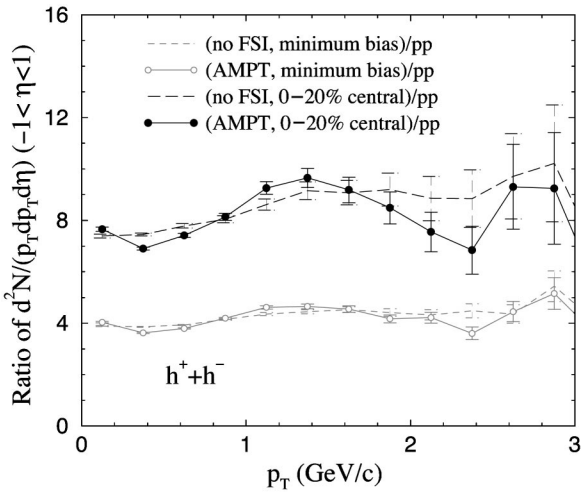

FIG. 7. Ratios of the charged particle transverse momentum spectra for d+Au collisions over the spectra for $p+p$ collisions from AMPT with (solid) or without (dashed) final-state interactions.

AMPT calculations shown in Fig. 7, either with or without final-state interactions, are much weaker. Thus, interactions in the final state are not the main reason for the observed strong p_T dependence of the ratios of transverse momentum spectra, suggesting that initial-state effects such as parton momentum broadening due to the Cronin effect [13,33] (not included in the AMPT model so far) are important in d+Au collisions.

For identified particles such as π^+, K^+, and protons, their transverse momentum spectra within the rapidity range of $-1<y<1$ from minimum-bias d+Au collisions are shown in Fig. 8, with the proton spectra scaled down by a factor of 10. Solid and dashed curves represent AMPT results with and without final-state interactions, respectively. Compared with results from the AMPT model on central heavy ion collisions, e.g., Fig. 2 of Ref. [3] for central Pb+Pb collisions at SPS, the effect of final-state interactions on the transverse momentum spectra in d+Au collisions are much weaker.

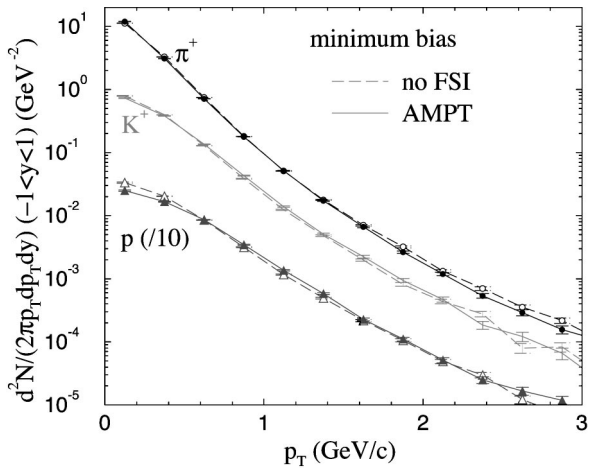

FIG. 8. Transverse momentum spectra of π^+, K^+, and protons from AMPT with (solid) or without (dashed) final-state interactions for minimum-bias d+Au collisions. The proton spectra are scaled down by a factor of 10.

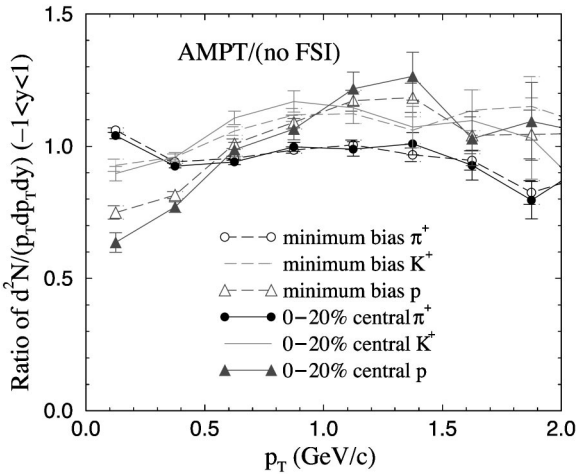

FIG. 9. Ratios of the transverse momentum spectra of π^+, K^+, and protons from AMPT over those from the AMPT model without final-state interactions for minimum-bias (dashed) and 0–20% central (solid) d+Au collisions.

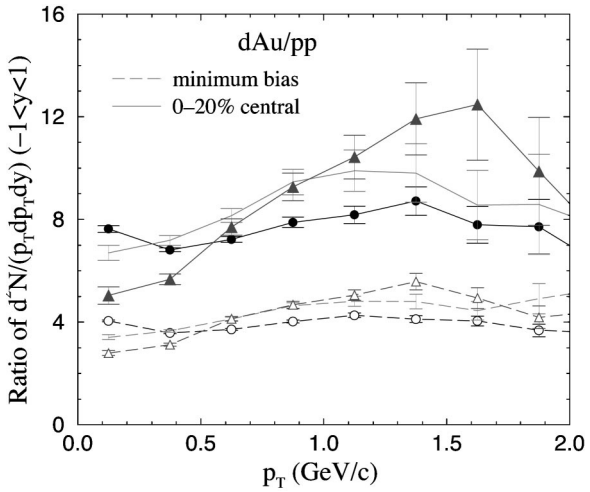

FIG. 10. Ratios of the transverse momentum spectra from AMPT for d+Au collisions over those for $p+p$ collisions. Solid and dashed curves correspond to 0–20% central and minimum-bias d +Au collisions, respectively.

Figure 9 shows the ratios of the p_T spectra from AMPT over those from the AMPT model without final-state interactions. Dashed curves represent the ratios of the minimum-bias spectra shown in Fig. 8, while solid curves represent the ratios of the spectra from 0 to 20% d+Au collisions. We see that final-state interactions modify the p_T spectra of π, K, and protons differently. Proton spectra show the largest FSI effect with low p_T protons shifting to higher p_T, and the ratio for 0–20% central events has a stronger p_T dependence than that for minimum-bias events. Both features are consistent with the existence of some transverse flow in d+Au collisions. We find that the average number of partonic collisions per parton is about 0.06 (with 3-mb parton scattering cross section) and the average number of hadronic collisions per produced hadron is about 1 in minimum-bias d+Au collisions from the AMPT model, compared with about 1 partonic collision per parton and 8 hadronic collisions per hadron in central Au +Au collisions at 200A GeV. As a result, the transverse flow due to final-state interactions in d+Au collisions is much weaker than in central heavy ion collisions. We also note that in the default AMPT model used in this study, final-state interactions among partons are less important than those among hadrons as only minijet partons are included in the parton cascade.

Ratios of the p_T spectra in d+Au collisions over those in $p+p$ collisions from the AMPT model are shown in Fig. 10. Similar to Fig. 9, we observe the strongest p_T dependence for protons. Also, ratios of the p_T spectra of kaons have a stronger p_T dependence than those of pions. We note that, since the initial-state parton broadening due to the Cronin effect [13] has not yet been included in the AMPT model, the p_T dependence of these ratios may get even stronger if the Cronin effect is taken into account.

C. Effects of the string fragmentation parameters and nuclear shadowing

In the default AMPT model, hadron production after the partonic phase is described by the Lund string fragmentation model. In this model, the longitudinal momentum distribution of a hadron with transverse mass $m_\perp$ produced from the string fragmentation is given by the following symmetric splitting function [27]:

$$f(z) \propto z^{-1}(1-z)^a \exp(-b\, m_\perp^2/z), \tag{2}$$

where z denotes the light-cone momentum fraction of the produced hadron with respect to that of the fragmenting string. In the HIJING model, which reproduces the experimental charged particle multiplicities in high energy $p+p$ and $p\bar{p}$ collisions, the default values of $a=0.5$ and $b=0.9$ GeV^{-2} are used. However, in order to reproduce the rapidity distributions of charged particles in central Pb +Pb collisions at the CERN-SPS energy using the AMPT model, we find that values of these parameters need to change to $a=2.2$ and $b=0.5$ GeV^{-2} [2,3]. The increase of a and decrease of b relative to the default values in the HIJING model soften the splitting function and thus enhance the total charged particle multiplicity by about 20% in central Pb+Pb collisions at SPS. The change of these two parameters can perhaps be attributed to the modification of string fragmentation when multiple strings are produced and overlap in heavy ion collisions, although it is not known yet how these parameters should be modified in different colliding systems. Since peripheral d+Au collisions are expected to behave similarly as $p+p$ collisions, and even in central d+Au collisions the string density is much lower than in central heavy ion collisions, we have assumed that the parameters a and b of Eq. (2) for deuteron-gold collisions have the same values as in $p+p$ collisions, i.e., they take the default values in the HIJING model.

However, since the values of a and b parameters need to be modified in order to describe the total multiplicity in central heavy ion collisions, it is still possible that these parameters are also modified in nonperipheral deuteron-gold collisions. If in central deuteron-gold collisions the parameters a

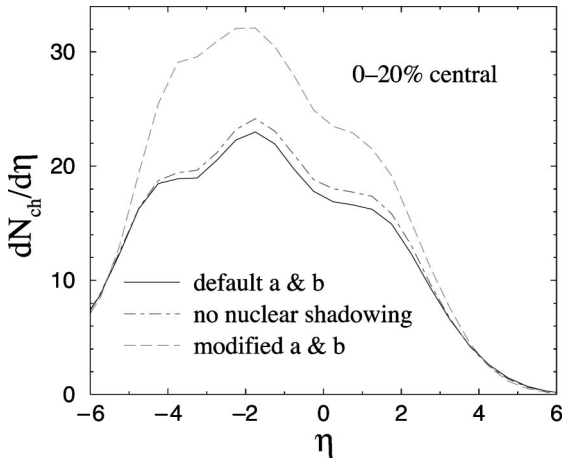

FIG. 11. Charged particles pseudorapidity distributions for the most central 20% deuteron-gold collisions from AMPT with default values of *a* and *b* parameters (solid), with nuclear shadowing turned off (dot-dashed), or with modified *a* and *b* values as in heavy ion collisions (dashed).

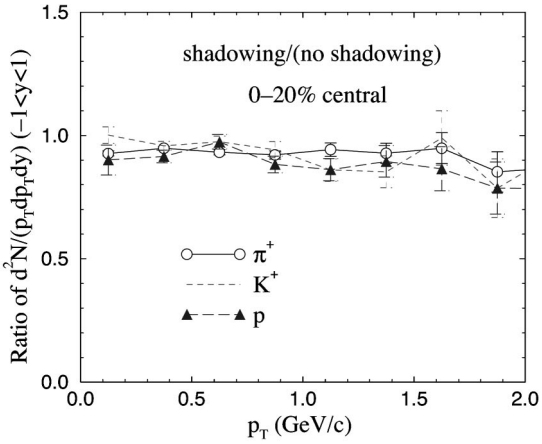

FIG. 12. Ratios of the transverse momentum spectra of π^+, K^+, and protons from AMPT with nuclear shadowing over those without nuclear shadowing for 0–20% central d+Au events.

and *b* already have the modified values as in heavy ion collisions, the pseudorapidity distribution for the 20% most central deuteron-gold collisions (selected from $N_{\rm part}$) would be given by the dashed curve in Fig. 11, which shows a substantial increase compared with the previous AMPT result obtained with default *a* and *b* values in the HIJING model (solid curve). Comparison of these results for deuteron-gold collisions with upcoming experimental results at RHIC will thus allow us to learn how the string fragmentation process is modified in different colliding systems or centralities.

When the nuclear shadowing effect is turned off in the AMPT model, the pseudorapidity distribution for the 20% most central deuteron-gold collisions is shown by the dot-dashed curve in Fig. 11, which is not much different from the solid curve obtained with the nuclear shadowing. Thus, pseudorapidity distributions of charged particles in deuteron-gold collisions are not very sensitive to the nuclear shadowing effect. This is different from that seen in collisions between heavy nuclei, where the effect is much larger as nuclear shadowing affects the production of minijet partons, which scales with the number of binary collisions. The effects of nuclear shadowing on $p_{\rm T}$ spectra of π^+, K^+, and protons, shown in Fig. 12 for 0–20% central d+Au collisions, are also relatively small and do not have a strong $p_{\rm T}$ dependence within $0<p_{\rm T}<3$ GeV/c. Note that, although the nuclear shadowing effect is unimportant for global observables in small colliding systems such as deuteron-gold collisions, it affects significantly observables which are dominated by partonic interactions such as open charm production [25] or the yield of high $p_{\rm T}$ particles.

IV. SUMMARY

Using a multiphase transport (AMPT) model that includes both final-state partonic and hadronic interactions, we have studied the pseudorapidity distributions of charged particles, their centrality dependence, and transverse momentum spectra of different particles in deuteron-gold collisions at $\sqrt{s_{NN}}=200$ GeV. Due to the asymmetry of these collisions, the centrality dependence of charged particle multiplicity per participant is very different at different pseudorapidities, and it goes from increasing with centrality at the backward pseudorapidity region (the fragmentation region of the gold nuclei) to decreasing with centrality at the forward region. The charged particle pseudorapidity distribution in central deuteron-gold collisions is also sensitive to the values of the parameters used in the string fragmentation function. Furthermore, we find that, although final-state partonic and hadronic interactions modify the transverse momentum spectra of charged particles in d+Au collisions relative to scaled $p+p$ collisions, the $p_{\rm T}$ dependence of the modification due to final-state interactions is much weaker than observed at RHIC. Thus, initial-state effects such as parton momentum broadening due to the Cronin effect are important in deuteron-gold collisions. However, we find that final-state interactions have a much stronger effect on the $p_{\rm T}$ spectra of protons than those of kaons or pions. Comparison of these predictions with the experimental data will thus help us to learn more about initial-state effects on transverse momentum spectra and to study whether string fragmentation is modified in deuteron-gold collisions as in central heavy ion collisions.

ACKNOWLEDGMENTS

We thank Ulrich Heinz, Peter Jacobs, and Michael Murray for valuable comments. This paper is based on work supported by the U.S. Department of Energy under Grant No. DE-FG02-01ER41190 (Z.W.L.) and by the U.S. National Science Foundation under Grant No. PHY-0098805 as well as the Welch Foundation under Grant No. A-1358 (C.M.K.).

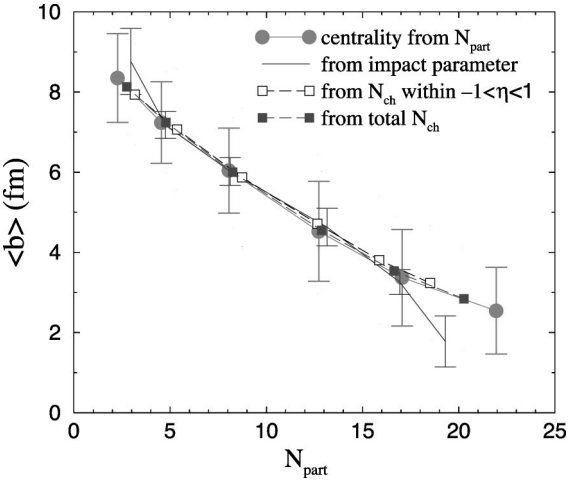

FIG. 13. The average value of impact parameter as a function of $N_{\rm part}$ with different criteria for the centrality selection, together with the rms width of the impact parameter in each centrality bin for two of the curves.

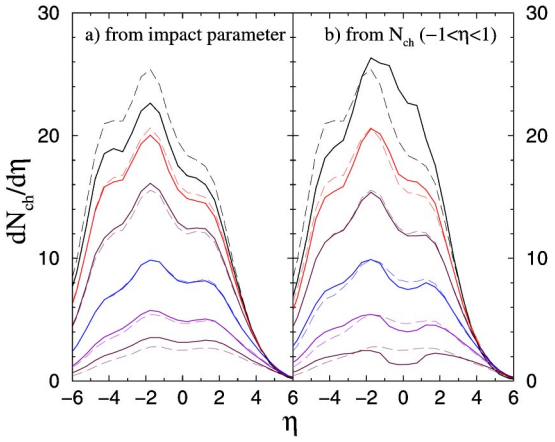

FIG. 14. Charged particle pseudorapidity distributions at six centrality bins of 0–10%, 10–20%, 20–40%, 40–60%, 60–80%, and 80–100% when the centrality is determined from a) the impact parameter or b) N_{ch} within $-1<\eta<1$. Dashed curves represent results when the centrality is determined from $N_{\rm part}$.

APPENDIX: EFFECTS OF DIFFERENT CENTRALITY SELECTIONS

To extract useful information from the centrality dependence of global observables, it is helpful to study how the criteria of centrality selection affects the centrality dependence. The number of participants and the impact parameter are known in theoretical models, but they cannot be directly measured in experiments. Instead, experimental centrality selections usually involve cutting on the charged particle multiplicity or the transverse energy. Thus, in addition to separating events into different centrality bins using the total number of participants, we have also tried three other methods, using the impact parameter, the number of charged particles within $-1<\eta<1$, and the total number of charged particles. For example, when the total number of charged particles is used for the centrality selection, we order all 35 000 events from the AMPT model by the total number of charged particles in each event. The centrality bin of, say 0–10%, then consists of the first 3 500 events in that ordered list.

In Fig. 13, we plot the average value of impact parameters versus the average value of $N_{\rm part}$ at six centrality bins of 0–10%, 10–20%, 20–40%, 40–60%, 60–80%, and 80–100% that are selected using these four different methods. The solid curve with circles corresponds to the centrality selection from $N_{\rm part}$, and it thus has the largest value of $N_{\rm part}$ for the most central bin of events and the smallest value of $N_{\rm part}$ for the most peripheral bin of events. On the other hand, the centrality selection from the impact parameter, shown by the solid curve with no symbols, has the smallest value of $\langle b\rangle$ for the most central bin of events and the largest value of $\langle b\rangle$ for the most peripheral bin of events. When the number of charged particles is used to determine the centrality, the correlation between the centrality and $N_{\rm part}$ is weaker than in the case of using $N_{\rm part}$. This is especially true when only part of the phase space is included, as using N_{ch} within $-1<\eta<1$ for the centrality selection (curve with open squares) leads to a narrower range of $N_{\rm part}$ than using the total number of charged particles for the centrality selection (curve with filled squares). The error bars shown for two of the curves in Fig. 13 (the curves from using $N_{\rm part}$ or impact parameter for the centrality selection) correspond to the root-mean-square widths of the impact parameters in each centrality bin, and we see that the width in the case of using $N_{\rm part}$ for determining the centrality is quite large (around 1.2 fm) for these centrality bins. We also find that, when N_{ch} within $-1<\eta<1$ or the total N_{ch} is used for the centrality selection, these widths are even larger (between 1.3 and 1.8 fm), indicating that the correlation between N_{ch} and the impact parameter is weaker than that between $N_{\rm part}$ and the impact parameter.

Different centrality selections also lead to differences in both the shape and magnitude of the pseudorapidity distributions at the same centrality bin. Solid curves in Figs. 14(a) and 14(b) show the pseudorapidity distributions of charged particles using, respectively, the impact parameter and N_{ch} within $-1<\eta<1$ for determining the centrality. The distri-

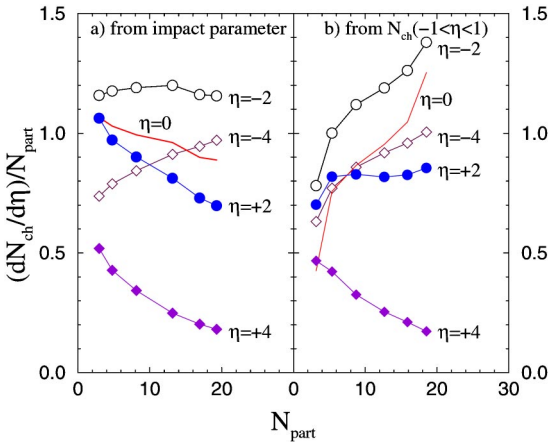

FIG. 15. Centrality dependence of charged particle multiplicity with the centrality determined from (a) the impact parameter or (b) N_{ch} within $-1<\eta<1$.

butions corresponding to using $N_{\rm part}$ for the centrality selection are also shown by the dashed curves for comparison. From Fig. 14(a), we find that $dN_{ch}/d\eta$ at $\eta=0$ grows slower with centrality when the impact parameter instead of $N_{\rm part}$ is used for the centrality selection. However, it is interesting to see, from comparing Fig. 15(a) with Fig. 5, that the centrality dependences of $(dN_{ch}/d\eta)/N_{\rm part}$ for the two cases are quite similar. This is due to the compensating effect of slower growth of $N_{\rm part}$ with centrality when the impact parameter is used to select the centrality (see Fig. 13). We note that in relativistic heavy ion collisions where the multiplicity is much higher, these different methods for the centrality selection lead to quite similar results, contrary to those shown in Figs. 13 and 14 for d+Au collisions.

Figure 15(b) shows the centrality dependence of charged particle multiplicity per participant at different pseudorapidities when N_{ch} within $-1<\eta<1$ is used for the centrality selection. Comparing with Fig. 5, we find that the centrality dependence at $\eta=-4$ or $\eta=+4$ is similar to the case where $N_{\rm part}$ determines the centrality, but the centrality dependence at $\eta=-2, 0$ or $+2$ is totally different. For example, while in Fig. 5 [and in Fig. 15(a)] the curve of $(dN_{ch}/d\eta)/N_{\rm part}$ at $\eta=0$ shows a small decrease with centrality, the corresponding curve in Fig. 15(b) increases significantly with centrality. We note that these differences from Fig. 5 exist even when the total number of N_{ch} is used for selecting the centrality (instead of N_{ch} within $-1<\eta<1$). Part of this large difference in the centrality dependence is due to the stronger increase of $dN_{ch}/d\eta(\eta=0)$ with centrality in the case when N_{ch} around midpseudorapidity is used to determine the centrality, as shown in Fig. 14(b). Also, since the average value of $N_{\rm part}$ grows slower with centrality in this case (see Fig. 13), the difference is further enhanced after dividing $dN_{ch}/d\eta$ by $N_{\rm part}$. Figures 14 and 15 thus show that the criteria of centrality selection can introduce appreciable differences in the centrality dependence of global observables in deuteron-gold collisions, and corresponding care must be taken when comparing theoretical results with experimental data on centrality dependences.

[1] B. Zhang, C. M. Ko, B. A. Li, and Z. W. Lin, nucl-th/9904075; Phys. Rev. C **61**, 067901 (2000).

[2] Z. W. Lin, S. Pal, C. M. Ko, B. A. Li, and B. Zhang, Phys. Rev. C **64**, 011902 (2001).

[3] Z. W. Lin, S. Pal, C. M. Ko, B. A. Li, and B. Zhang, Nucl. Phys. **A698**, 375 (2002).

[4] B. Zhang, C. M. Ko, B. A. Li, Z. W. Lin, and B. H. Sa, Phys. Rev. C **62**, 054905 (2000); B. Zhang, C. M. Ko, B. A. Li, Z. W. Lin, and S. Pal, *ibid.* **65**, 054909 (2002).

[5] S. Pal, C. M. Ko, and Z. W. Lin, nucl-th/0106073; Nucl. Phys. **A707**, 525 (2002).

[6] Z. W. Lin and C. M. Ko, Phys. Rev. C **65**, 034904 (2002).

[7] Z. W. Lin, C. M. Ko, and S. Pal, Phys. Rev. Lett. **89**, 152301 (2002).

[8] K. H. Ackermann *et al.*, STAR Collaboration, Phys. Rev. Lett. **86**, 402 (2001).

[9] C. Adler *et al.*, STAR Collaboration, Phys. Rev. Lett. **87**, 082301 (2001).

[10] X. N. Wang and M. Gyulassy, Phys. Rev. D **44**, 3501 (1991).

[11] X. N. Wang and M. Gyulassy, Phys. Rev. D **45**, 844 (1992).

[12] M. Gyulassy and X. N. Wang, Comput. Phys. Commun. **83**, 307 (1994).

[13] J. W. Cronin, H. J. Frisch, M. J. Shochet, J. P. Boymond, R. Mermod, P. A. Piroue, and R. L. Sumner, Phys. Rev. D **11**, 3105 (1975).

[14] B. Zhang, Comput. Phys. Commun. **109**, 193 (1998).

[15] D. Molnar and M. Gyulassy, Phys. Rev. C **62**, 054907 (2000).

[16] P. F. Kolb, P. Huovinen, U. W. Heinz, and H. Heiselberg, Phys. Lett. B **500**, 232 (2001).

[17] P. Huovinen, P. F. Kolb, U. W. Heinz, P. V. Ruuskanen, and S. A. Voloshin, Phys. Lett. B **503**, 58 (2001).

[18] P. F. Kolb, U. W. Heinz, P. Huovinen, K. J. Eskola, and K. Tuominen, Nucl. Phys. **A696**, 197 (2001).

[19] D. Teaney, J. Lauret, and E. V. Shuryak, nucl-th/0110037.

[20] D. Kharzeev and E. Levin, Phys. Lett. B **523**, 79 (2001).

[21] D. Kharzeev and M. Nardi, Phys. Lett. B **507**, 121 (2001).

[22] D. Kharzeev, E. Levin, and M. Nardi, hep-ph/0212316.

[23] K. J. Eskola, K. Kajantie, P. V. Ruuskanen, and K. Tuominen, Nucl. Phys. **B570**, 379 (2000); Phys. Lett. B **543**, 208 (2002).

[24] K. J. Eskola, K. Kajantie, and K. Tuominen, Phys. Lett. B **497**, 39 (2001).

[25] Z. W. Lin and M. Gyulassy, Phys. Rev. Lett. **77**, 1222 (1996).

[26] T. Sjostrand, Comput. Phys. Commun. **82**, 74 (1994).

[27] B. Andersson, G. Gustafson, and B. Soderberg, Z. Phys. C **20**, 317 (1983); B. Andersson, G. Gustafson, G. Ingelman, and T. Sjostrand, Phys. Rep. **97**, 31 (1983).

[28] B. A. Li and C. M. Ko, Phys. Rev. C **52**, 2037 (1995).

[29] L. Hulthén and M. Sugawara, *Handbuch der Physik* (Springer-Verlag, Berlin, 1957), Vol. 39, p. 33.

[30] This form of the Hulthen function has been implemented in version 1.383 of the HIJING model.

[31] The popcorn mechanism is controlled mainly by parameters MSTJ(12) and PARJ(5) in the PYTHIA/JETSET program.

[32] S. S. Adler *et al.*, PHENIX Collaboration, Phys. Rev. Lett. **91**, 072303 (2003); J. Adams *et al.*, STAR Collaboration, *ibid.* **91**, 072304 (2003); B. B. Back *et al.*, PHOBOS Collaboration, *ibid.* **91**, 072302 (2003); I. Arsene *et al.*, BRAHMS Collaboration, *ibid.* **91**, 072305 (2003).

[33] I. Vitev, Phys. Lett. B **562**, 36 (2003).